Biological fingerprint using scout computed tomographic images for positive patient identification

First author (corresponding author)

Name: Yasuyuki Ueda

Institution:

Division of Health Sciences, Graduate School of Medicine, Osaka University

E-mail: ueda@sahs.med.osaka-u.ac.jp

Work telephone number: +81-6-6879-2443

Work fax number: none

Postal address: 1-7 Yamadaoka, Suita, Osaka 565-0871, Japan

Second author

Name: Junji Morishita

Institution:

Department of Health Sciences, Faculty of Medical Sciences, Kyushu University

E-mail: junjim@med.kyushu-u.ac.jp

Work telephone number: +81- 92-642-6673

Work fax number: none

Postal address: 3-1-1, Maidashi, Higashi-ku, Fukuoka 812-8582, Japan

Third author

Name: Tadashi Hongyo

Institution:

Division of Health Sciences, Graduate School of Medicine, Osaka University

E-mail: hongyo@sahs.med.osaka-u.ac.jp

Work telephone number: +81-6- 6879-2562

Work fax number: none

Postal address: 1-7 Yamadaoka, Suita, Osaka 565-0871, Japan

Abstract

Purpose: Management of patient identification is an important issue that should be addressed to ensure patient safety while using modern healthcare systems. Patient identification errors can be mainly attributed to human errors or system problems. An error-tolerant system, such as a biometric system, should be able to prevent or mitigate potential misidentification occurrences. Herein, we propose the use of scout computed tomography (CT) images for biometric patient identity verification and present the quantitative accuracy outcomes of using this technique in a clinical setting.

Methods: Scout CT images acquired from routine examinations of the chest, abdomen, and pelvis were used as biological fingerprints. We evaluated the resemblance of the follow-up with the baseline image by comparing the estimates of the image characteristics using local feature extraction and matching algorithms. The verification performance was evaluated according to the receiver operating characteristic (ROC) curves, area under the ROC curves (AUC), and equal error rates (EER). The closed-set identification performance was evaluated according to the cumulative match characteristic curves and rank-one identification rates (R1).

Results: A total of 619 (383 males, 236 females, age range 21–92 years) patients who

underwent baseline and follow-up chest-abdomen-pelvis CT scans on the same CT

20 system were analyzed for verification and closed-set identification. The highest

performances of AUC, EER, and R1 were 0.998, 1.22%, and 99.7%, respectively, in the

considered evaluation range. Furthermore, to determine whether the performance

decreased in the presence of metal artifacts, the patients were classified into two

groups, namely scout images with (255 patients) and without (364 patients) metal

25 artifacts, and the significance test was performed for two ROC curves using the

unpaired Delong's test. No significant differences were found between the ROC

performances in the presence and absence of metal artifacts when using a sufficient

number of local features. Our proposed technique demonstrated that the

performance was comparable to that of conventional biometrics methods when

30 using chest, abdomen, and pelvis scout CT images. Thus, this method has the

potential to discover inadequate patient information using the available chest,

abdomen, and pelvis scout CT image; moreover, it can be applied widely to routine

adult CT scans where no significant body structure effects due to illness or aging are

present.

35 Conclusions: Our proposed method can obtain accurate patient information

available at the point-of-care and help healthcare providers verify whether a

patient's identity is matched accurately. We believe the method to be a key solution

for patient misidentification problems.

Keywords:

1. Introduction

A patient's identity should be verified prior to clinical examinations or treatments to ensure that the correct patient undergoes all the relevant medical practices [1-5]. Many hospitals rely on manual processes and name tags, such as a wristband with a barcode, to identify patients during registration [2-5]. Identification procedures, such as the use of at least two patient identifiers are often adopted (e.g., name and date of birth); however, these confirmations are not always foolproof [1-5]. Healthcare providers may struggle to collect precise patient information and match individuals to their medical records. There are several human factors that can cause patient misidentification, including communication or human errors in healthcare work [6]. While human error is innate in our nature, some human errors can be avoided [6]. Healthcare providers can practice patient confirmation processes to ensure that they are examining the correct patient. However, this may increase their workloads. In addition to conventional patient confirmation, to use of biometrics for automated patient identity verification can be expected to reduce patient misidentification problems [7].

The term biometrics refers to the use of behavioral and biological characteristics to identify an individual [8-27]. Biometrics are utilized as a part of either a verification

60   or an identification system [11-27]. Biometric verification refers to the authentication

of a patient's identity by comparing a biological fingerprint with one pre-stored in a

database [8-10]. Patient verification is a crucial means to ascertain the correctness

of a patient's identity. Biometric verification process for healthcare authenticates a

patient's identity in addition to the manual checking conducted by healthcare

65   providers [11-15]. Biometric identification usually refers to the closed-set identification

of someone whose biological fingerprint is stored in a database [8-10]. Patient

identification is a crucial means to identify unconscious or unknown patients [25-27].

We have previously reported on the usefulness of biological fingerprints using scout

magnetic resonance (MR) images of the brain [11]. In other previous studies, medical

70   image biometrics were reported using chest [19-22, 25-27] and knee [23] X-ray

images, optical surface images [13], and patient X-ray images [24] acquired during

a radiotherapy set-up process, facial images[15] extracted from computed

tomography (CT), and facial images[12, 14] acquired with mobile camera.

Biometrics for healthcare preferred to be a simple process to enable identity

75   verification under various patient conditions [1-5]. Furthermore, although additional

biometric input devices were used to acquire and process patient characteristics in

some studies [12-14], it is desirable to avoid such additional devices for appropriate

handling of private information.

Biological fingerprint techniques using scout images have high versatility for

80   verifying a patient's identity [11]. Scout images are preliminary image sets that are

routinely obtained for localization to determine ranges in CT or MR imaging

examinations. Consequently, it is possible to verify the identity of a patient using only

some existing scout images. Therefore, there is no need to separately scan a patient

to obtain characteristic data for biometrics. Additionally, if we can set all the

85   parameters required for biometrics in advance, the verification process can be

executed automatically during a clinical imaging. Thus, use of scout image based

biometrics makes the process convenient at both the healthcare provider side and

patient side. However, this technique is not applicable to other imaging methods.

Nevertheless, verification of the patient identity during CT examination as well as

90   chest X-ray and head MR imaging examinations is important. We believe that a

biological fingerprint technique can be used as a patient confirmation tool during

frequently performed CT examinations. The purpose of our study is to a) use scout CT

images from the chest, abdomen, and pelvis for patient identity verification during

CT examinations to avoid performing a CT scan on the wrong patient, and b) present

95   quantitatively accurate outcomes using this technique in a clinical setting.

2. Materials and Methods

2.1. Subjects:

This study was conducted as a retrospective, observational study and was approved by the Institutional Review Boards at Osaka University and Yamaguchi University Hospital. Written informed consent was not required owing to the retrospective design of this study. All procedures conducted herein were in conformance with the Declaration of Helsinki.

This study used the scan information from 619 patients who underwent two chest-abdomen-pelvis CT scans between May 2015 and May 2016 at the Yamaguchi University Hospital in Japan. Patients under the age of 20 years, those who have intravenous iodined contrast administration, and those who did not undergo the exams in the required supine position with their arms raised were excluded. All scout scans were performed using a CT system (SOMATOM Sensation 64, Siemens Medical Solutions, Forchheim, Germany). Furthermore, a preliminary study of different CT system models was performed for a patient who underwent three chest-abdomen-pelvis CT examinations, i.e., two baseline scans acquired using SOMATOM Sensation and Definition (both Siemens Medical Solutions, Forchheim, Germany) and a follow-up scan acquired using SOMATOM Sensation. **Error! Reference source not found.**

shows the patient characteristics of this study. **Error! Reference source not found.**

115   shows the scan parameters of the scout CT.

Figure 1 shows the scanning geometry of the chest-abdomen-pelvis scout CT scan.

2.2. Methodology:

2.2.1.   Outline:

Figure 2 shows the flowchart for the biological fingerprint verification framework of

120   our method. The procedure comprises four major steps, namely a) geometric

correction, b) local feature extraction, c) valid correspondence evaluation, and d)

similarity evaluation. Biological fingerprint processing was performed using MATLAB

version R2018a (MathWorks Inc., 2018) on Windows 10.

2.2.2. Geometric correction

125   The projected patient transverse size of the scout CT image varies with the scanner

table height owing to geometric effects. The geometric effects of changing the

table height can be calculated using the method of similar triangles. The geometric

correction factor at the height of the rotation center can be parameterized as

follows:

130    $a = \dfrac{D_{So}}{D_{So} + TH}$,

where a denotes the magnification factor in the transverse direction, D_{so} denotes

the distance from the focal spot in the X-ray tube to the rotation center, and the

table height, TH, denotes the distance from the couch to the rotation center.

Accordingly, all scout CT images are processed for correction to cancel this

135   geometric error. Figure 3a shows the original follow-up scout CT image, and Fig. 3(b-

d) shows the cropped processing area of the images after geometric correction.

2.2.3. Local feature extraction:

Each initial local feature point is used as the center for defining the

corresponding square regions of interest (ROI) based on which the template

140   images of the follow-up scout CT images are obtained. An initial local feature point

algorithm [28] uses the following two steps. First, local maxima are computed using

the data in the follow-up scout image recorded only within the couch area.

Specifically, the local maxima are the points that are strictly larger in value than all

other pixels in a 3 × 3 neighborhood. The local maxima are then sorted in a

145   descending order according to the peak value, and the coordinates of the first N

local maxima are obtained as the initial local feature points.

    We consider that validating the computational cost and performance

depending on the number of the initial local feature points and template matrix

sizes is necessary. Figures 3b, 3c, and 3d, show examples corresponding to N=100,

150   200, and 300, respectively, of the initial local feature point set. In addition, Figs 3f,

3g, and 3h, show examples of including metal artifact corresponding to N=100, 200,

and 300, respectively, of the initial local feature point set.

2.2.4.   Valid correspondence evaluation

Local corresponding points were computed using the template matching

155   technique via normalized cross-correlation [30] between the follow-up and the

baseline scout CT images. The template matching technique, which is a feature

point tracking method, is used to identify the corresponding pairs linked to the initial

local feature point set O in the follow-up scout CT image. A local corresponding point

set P is thus obtained in the baseline scout CT image. Each local corresponding point

160   set P is used as the center for a square ROI according to which the template images

of the baseline scout CT image are obtained. The template matching technique is

executed again to find the corresponding pairs linked to the local corresponding

point set P in the baseline scout CT image. Accordingly, the final local feature point

of the follow-up scout CT image O' is obtained.

165   ### 2.2.5.   Similarity evaluation

To examine the resemblance, we determined the correspondence rate, C, using

the following equations:

$$C = \frac{M}{N},$$

$$M = |Q|,$$

170     $$Q = (O \cap O'),$$

$N = |O|.$

Let M and N be the numbers of respective feature points Q and O. Additionally, let Q be the valid corresponding feature point that consists of all the elements in which the distance between O and O' is within two pixels. If the correspondence rate is less than the threshold value, the estimation of the follow-up and baseline scout CT images is identified as an impostor (different patient) pair. Otherwise, the estimations of the follow-up and baseline scout CT images are accepted as a genuine (same patient) pair.

2.3. Performance evaluation

The verification performance of our method was evaluated in terms of the receiver operating characteristic (ROC) curve and its corresponding equal error rates (EERs) and area under the ROC curves (AUCs). The EER on the ROC curve indicates the point that has an equal probability for the misclassification of the genuine- or impostor pairs. In a good biometric system, the EER should be as low as possible [28]. The unpaired DeLong's test [31, 32] was used to evaluate the AUCs between two groups classified as including (255 patients) or not including (364 patients) metal artifacts. In the ROC analysis, the number of impostor pairs was reduced by using random sampling to make the numbers of genuine and impostor pairs the same. P

values of < 0.05 were considered statistically significant. Statistical analysis was

190   performed using the computing environment R version 3.6.0 (R Development Core

Team, 2019) on Windows 10.

The closed-set identification performance of our method was evaluated in terms

of the cumulative match characteristic (CMC) curve and its rank-one identification

rate (R1). The true-positive identification rate is the proportion of correctly matched

195   identifications contained within the top R matches, where R is the rank. [28] The CMC

curve is used to evaluate the true-positive identification rate within the top R matches

[28]. Thus, R1 indicates that the rank of the genuine patient pair is higher than that of

all impostor patient pairs. The higher the value of R1 is, the better the biometric system

is for closed-set identifications.

200   ## 3. Results

Figure 4 shows scout CT image examples of genuine and impostor pair analyses.

The correspondence rates achieved are 80.6% for the genuine pair and 18.0% for the

impostor pair. The correspondence rate is a characteristic factor for distinguishing

genuine matches from impostor matches. If each point correspondence is correct,

205   all lines connecting each valid corresponding feature point should be parallel.

Therefore, a non-parallel line connecting each valid corresponding feature point

represents incorrect point correspondence. Thus, the correspondence rate is higher

for genuine matches than it is for impostor matches. In addition,

Figure **5** shows an example of a scout CT image of an impostor pair comparison

210   with a correspondence rate of 44.3%. The obtained result demonstrates the potential

risk for misclassification of this dataset as a genuine pair (i.e., as a false acceptance

case). Furthermore, Figure 6 shows low correspondence rate examples for a genuine

pair evaluation due to a) patient's body posture translocations and b) a residual

contrast medium in the gastrointestinal tract at a follow-up scan, where the

215   correspondence rates were determined to be 15.0 and 33.3%, respectively. We

believe that several intra-patient temporal changes such as physical abnormalities,

body posture translocations, and metal artifacts may affect the performance of our

method. Figure 7 shows examples of scout CT images for analyses of same and different CT systems. The correspondence rates achieved are 58.7% for the same CT

220 system and 61.0% for a different CT system. The correspondence rate for the same CT system had an average value of 65.4 ± 16.3% for 619 patients.

Figure **8** shows the ROC curves for an initial local feature point set size of 300; the template matrix size of 16 × 16 showed the most successful performance with an AUC

225 of 0.998, and an EER of 1.22%. This was followed by the template matrix sizes of 32 × 32 (AUC of 0.997 and EER of 1.68%), and of 8 × 8 (AUC of 0.996 and EER of 1.62%). The template matrix size of 64 × 64 exhibited the poorest performance in the ROC analyses; nevertheless, our method achieved AUC and EER values of 0.989 and 3.77%, respectively. Figure 9 shows the CMC curves for an initial local feature point set size

230 of 300; the template matrix size of 16 × 16 produced the most successful performance, in which R1 was 99.7%. This was followed by the template matrix sizes of 8 × 8 and 32 × 32, for which R1 was 99.0 %. The template matrix size of 64 × 64 gave the poorest performance in the CMC analyses; nevertheless, our method achieved R1 values of 95.6%.

235 Figure 10 shows a comparison of the performance values, where a) is the EER on

the verification performance and b) is the R1 on the closed-set identification performance at various numbers of initial local feature points (50 - 300) for the four template matrix sizes. For all template matrix sizes, as the number of initial local feature points increased, the EER decreased gradually, while the R1 increased

240   gradually. The template matrix size of 16 × 16 yielded the best verification and closed-set identification performances among the four different template matrix sizes studied herein for different numbers of initial local feature points.

As shown in Figure 3a-3d, the unique image features used for the identification of individual patients in our method were mainly detected in the thoracic-lumbar spine,

245   mediastinum, lung boundary, and pelvic brim regions. However, the local maxima employed as the initial local feature point may be concentrated on a high contrast part under a patient's scout CT image, and a metal artifact example is shown in Figure 3e-3h. The actual local feature extraction processes using the top-100, top-200, and top-300 peaks of the local maxima is shown in Figure 3f, 3g, and 3h,

250   respectively. More specifically, in Figure 3f, the majority of the 100 initial local feature points appear to be concentrated on a specific gastrointestinal tract with residual contrast medium, in which it could be difficult to identify the individual patients. **Error! Reference source not found.** shows the AUCs and p values classified by whether the

scout CT image includes a metal artifact or not at the follow-up CT scan. Significant

255 differences were observed between the ROC performances at 100 and 200 initial

local feature points of the scout CT images with and without metal artifacts for the

unpaired Delong's test ($p < 0.05$). However, there were no significant differences

between the ROC performances at 300 initial local feature points of the scout CT

images with and without metal artifacts for the unpaired Delong's test. We, therefore,

260 believe that it is necessary to increase the number of initial local feature points in

regard to a patient where metal artifacts are observed in the follow-up scout CT

image as shown in Figure 6b. We note that our method of using 300 initial local

feature points exhibits high performance levels both in the presence and absence

of a metal artifact in the scout CT image.

265 **4. Discussion**

In this study, we have proposed a novel biological fingerprint technique using scout CT images from the chest, abdomen, and pelvis under a clinical setting. Our method is innovative because verification of the patient's identity is possible without using other biometric input devices if scout CT scan is acquired, and subjecting a

270 wrong patient to CT scan can be avoided during CT examination.

The evaluations demonstrated the effectiveness of the proposed technique for the identification and verification of patients using scout CT images as the biological fingerprint. Our method achieved AUC, EER, and R1 values of 0.998, 1.22%, and 99.7%, respectively, for a template matrix size of 16 × 16 and 300 initial local feature points.

275 In previous research by Shimizu et al. [20] and KAO et al. [22], the highest AUC values for biometric verifications from chest X-ray images were 0.994 and 0.963 ± 0.002, respectively. Furthermore, for biometrics based on scout MR images, Ueda et al. [11] achieved the highest AUC of 0.998, EER of 1.37%, and R1 of 98.6%. Thus, our method yielded identification and verification performances equivalent to the conventional

280 methods.

Our result indicated that optimal parameter settings for the template matrix size and the number of initial local feature points are 16 × 16 and 300, respectively. We

considered that the optimal matrix size should be 16 × 16 because the patient's body posture on the couch changes slightly at each scan in a routine CT examination. As

285 the cause of the performance degradation with template matrix sizes greater than or equal to 32 × 32, it is conceivable that a wider range of corresponding points was searched when the template matrix size was increased. Furthermore, a template matrix size of 8 × 8 is too small to be able to distinguish each patient's characteristics.

The performance of our method improved monotonically with increase in the

290 number of initial local feature points. Furthermore, for the number of initial local feature points of 300 and template matrix size of 16 × 16, the AUC values with and without metal artifacts were 0.998 and 0.999, respectively, and hence there was no significant difference. However, on changing the number of initial local feature points to 200 or less, there were significant differences between the groups with and

295 without metal artifacts ($P < 0.05$). The overall performance of our method may change when used for a database that contains data of patients from follow-up scan with various physical abnormalities, i.e., trauma, installed clinical metallic devices, and a contrasting medium included in the body. However, we considered that the results obtained with the optimal template matrix size (16 × 16) and sufficient

300 number (300 or more) of initial local feature points would not be affected

substantially, except for cases where systemic changes have occurred, such as trauma in Figure 6a.

There are limitations associated with our study. Our method requires the following between prior and current scans: existing and parseable scout images, use of the same equipment, same image quality, and a time period that does not significantly affect the whole structure of the patient due to aging.

This study is a retrospective analysis performed on a single CT system with the same acquisition parameters. Another limitation is that our database has a short-term follow-up period of thirteen months. This is because 619 patients were scanned in the period of May 2015 to May 2016, and the effect of change in aging could not be evaluated in our study. Consequently, we have not evaluated long-term changes and the effect of using different CT systems. These limitations hindered the confirmation of our method's applicability in a wide range of sites.

If the CT system is different, several geometrical settings and digital values of the scout CT image also differ. Furthermore, with age, loss of calcium occurs in bones; thus, the digital value of the scout CT image is expected to decrease. In addition, the effect of changes in body habitus are also related to age (secular trend). However, as shown in Figure 7, our preliminary study using different CT systems

achieved a correspondence rate of 61.0%. We believe that this result was equivalent

320   level to 58.7% for the same CT system, and also within the equivalent range of 65.4 ±

16.3% for an average correspondence rate for the same CT system. Hence, we

believe that the geometrical correction of our methodology is applicable even if a

patient is scanned with different CT systems. Moreover, it is assumed that age-related

changes in the human skeletal structure have a negligible contribution to scout CT

325   images. We believe that the local feature extraction, which mainly extracts the

human skeletal structure, and the valid correspondence evaluation of our

methodology are also minimally affected by the performance of our method, even

with variations in acquisition parameters, body habitus, and aging.

Although repeated follow-up research is needed over longer time periods and with

330   the use of a variety of scan conditions, we think that both age-related changes and

acquiring a different CT system do not affect the performance of our method. Thus,

we believe that our proposed method is a novel approach that can be applied in

biological fingerprint analysis based on the use of scout CT patient images from the

chest, abdomen, and pelvis.

335 **5. Conclusions**

In this study, we have proposed an innovative biological fingerprint technique using scout CT images that are easily available from routine chest, abdomen, and pelvis CT scans. Furthermore, it is possible to collect precise patient information and match individuals to their medical records without disrupting both patient

340 convenience and the primary tasks of healthcare provider. We consider that our method for chest abdomen, and pelvis CT examinations will provide a key solution to prevent patient misidentification attributed to human errors.

6. Acknowledgments

7. Conflicts of Interest

The authors have no relevant conflicts of interest to disclose.

350 **8. References**

1. Bittle MJ, Charache P, Wassilchalk DM. Registration-associated patient misidentification in an academic medical center: causes and corrections. Jt Comm J Qual Patient Saf. 2007;33(1):25-33. doi:10.1016/S1553-7250(07)33004-3

2. Danaher LA, Howells J, Holmes P, Scally P. Is it possible to eliminate patient

355 identification errors in medical imaging? J Am Coll Radiol. 2011;8(8):568-574. doi:10.1016/j.jacr.2011.02.021.

3. Henneman PL, Fisher DL, Henneman EA, Pham TA, Campbell MM, Nathanson BH. Patient identification errors are common in a simulated setting. Ann Emerg Med. 2010;55(6):503-509. doi:10.1016/j.annemergmed.2009.11.017.

360 4. Schulmeister L. Patient misidentification in oncology care. Clin J Oncol Nurs. 2008;12(3):495-498. doi:10.1188/08.CJON.495-498.

5. Snyder ML, Carter A, Jenkins K, Fantz CR. Patient misidentifications caused by errors in standard bar code technology. Clin Chem. 2010;56(10):1554-1560. doi:10.1373/clinchem.2010.150094.

365   6.   Medicine Io. To Err Is Human: Building a Safer Health System. Washington, DC:

             The National Academies Press; 2000. doi:10.17226/9728.

        7.   Bennardello F, Fidone C, Cabibbo S, Calabrese S, Garozzo G, Cassarino G,

             Antolino A, Tavolino G, Zisa N, Falla C, Drago G, Di Stefano G, Bonomo P. Use of

             an identification system based on biometric data for patients requiring

370   transfusions guarantees transfusion safety and traceability. Blood Transfus.

             2009;7(3):193-203. doi:10.2450/2009.0067-08.

        8.   An Introduction to Biometric Data Analysis. In: Dunstone T, Yager N, eds.

             Biometric System and Data Analysis: Design, Evaluation, and Data Mining.

             Boston, MA: Springer US; 2009:3-26. doi:10.1007/978-0-387-77627-9_1.

375   9.   Newman R. Security and Access Control Using Biometric Technologies:

             Application, Technology, and Management. Course Technology Press; 2009.

        10. Council NR. Biometric Recognition: Challenges and Opportunities. Washington,

             DC: The National Academies Press; 2010. doi:10.17226/12720.

11. Ueda Y, Morishita J, Kudomi S, Ueda K. Usefulness of biological fingerprint in

380   magnetic resonance imaging for patient verification. Med Biol Eng Comput.

2016;54(9):1341-1351. doi:10.1007/s11517-015-1380-x.

12. Silverstein E, Snyder M. Implementation of facial recognition with Microsoft

Kinect v2 sensor for patient verification. Med Phys. 2017;44(6):2391-2399.

doi:10.1002/mp.12241.

385   13. Wiant DB, Verchick Q, Gates P, et al. A novel method for radiotherapy patient

identification using surface imaging. J Appl Clin Med Phys. 2016;17(2):271-278.

doi:10.1120/jacmp.v17i2.6066.

14. Jeon B, Jeong B, Jee S, Huang Y, Kim Y, Park GH, Kim J, Wufuer M, Jin X, Kim SW,

Choi TH. A Facial Recognition Mobile App for Patient Safety and Biometric

390   Identification: Design, Development, and Validation. JMIR Mhealth Uhealth.

2019;7(4):e11472. doi:10.2196/11472.

15. Parks CL, Monson KL. Automated facial recognition of computed tomography-

derived facial images: patient privacy implications. J Digit Imaging.

2017;30(2):204–14. doi:10.1007/s10278-016-9932-7.

395   16. Belgacem N, Fournier R, Nait-Ali A, Bereksi-Reguig F. A novel biometric

authentication approach using ECG and EMG signals. J Med Eng Technol.

2015;39(4):226-238. doi:10.3109/03091902.2015.1021429.

17. Jekova I, Krasteva V, Schmid R. Human Identification by Cross-Correlation and

Pattern Matching of Personalized Heartbeat: Influence of ECG Leads and

400   Reference Database Size. Sensors (Basel). 2018;18(2). doi:10.3390/s18020372.

18. Koike-Akino T, Mahajan R, Marks TK, et al. High-accuracy user identification

using EEG biometrics. Conf Proc IEEE Eng Med Biol Soc. 2016;2016:854-858.

doi:10.1109/EMBC.2016.7590835.

19. Morishita J, Katsuragawa S, Sasaki Y, Doi K. Potential usefulness of biological

405   fingerprints in chest radiographs for automated patient recognition and

identification. Acad Radiol. 2004;11(3):309-315. doi:10.1016/S1076-

6332(03)00655-X

20. Shimizu Y, Matsunobu Y, Morishita J. Evaluation of the usefulness of modified

biological fingerprints in chest radiographs for patient recognition and

410   identification. Radiol Phys Technol. 2016;9(2):240-4. doi:10.1007/s12194-016-

0355-4.

21. Shimizu Y, Morishita J. Development of a method of automated extraction of biological fingerprints from chest radiographs as preprocessing of patient recognition and identification. Radiol Phys Technol. 2017;10(3):376-381.

415   doi:10.1007/s12194-017-0400-y.

22. Kao EF, Lin WC, Jaw TS, Liu GC, Wu JS, Lee CN. Automated patient identity recognition by analysis of chest radiograph features. Acad Radiol. 2013;20(8):1024-31. doi:10.1016/j.acra.2013.04.006.

23. Shamir L, Ling S, Rahimi S, Ferrucci L, Goldberg IG. Biometric identification using

420   knee X-rays. Int J Biom. 2009;1(3):365-370. doi:10.1504/IJBM.2009.024279.

24. Lamb JM, Agazaryan N, Low DA. Automated patient identification and localization error detection using 2-dimensional to 3-dimensional registration of kilovoltage x-ray setup images. Int J Radiat Oncol Biol Phys. 2013;87(2):390-3. doi:10.1016/j.ijrobp.2013.05.021.

425   25. Morishita J, Katsuragawa S, Kondo K, Doi K. An automated patient recognition method based on an image-matching technique using previous chest radiographs in the picture archiving and communication system environment. Med Phys. 2001;28(6):1093-1097. doi:10.1118/1.1373403.

26. Morishita J, Watanabe H, Katsuragawa S, et al. Investigation of misfiled cases in

430   the PACS environment and a solution to prevent filing errors for chest

radiographs. Acad Radiol. 2005;12(1):97-103. doi:10.1016/j.acra.2004.11.008.

27. Toge R, Morishita J, Sasaki Y, Doi K. Computerized image-searching method for

finding correct patients for misfiled chest radiographs in a PACS server by use of

biological fingerprints. Radiol Phys Technol. 2013;6(2):437-43.

435   doi:10.1007/s12194-013-0221-6.

28. ISO. ISO/IEC 19795-1:2006 Information technology - Biometric Performance

Testing and Reporting - Part 1: Principles and Framework; 2006.

29. Vincent L, Dougherty ER. Morphological segmentation for textures and

particles. In: Dougherty ER (Ed.), Digital Image Processing Methods, Marcel

440   Dekker, New York. 1994:43-102.

30. Briechle K, Hanebeck UD. Template matching using fast normalized cross

correlation. Proc. SPIE, vol. 4387, pp. 95-102, 2001. doi: 10.1117/12.421129.

31. DeLong ER, DeLong DM, Clarke-Pearson DL. Comparing the areas under two or more correlated receiver operating characteristic curves: a nonparametric approach. Biometrics. 1988;44(3):837-45. doi:10.2307/2531595.

32. Robin X, Turck N, Hainard A, Tiberti N, Lisacek F, Sanchez JC, Müller M. pROC: an open-source package for R and S+ to analyze and compare ROC curves. BMC Bioinformatics. 2011;12:77. doi:10.1186/1471-2105-12-77.

445

Figure Legends

Figure 1 Scan geometry of the chest-abdomen-pelvis scout CT scan. Scout CT images are acquired with the patient in the supine position with his/her arms raised above his/her head. The couch is translated at constant speed through the gantry opening during X-ray acquisition. The X-ray tube and detector array do not rotate around the patient during scout image acquisition. D_{so}: distance from the focal spot in the X-ray tube to the rotation center, table height (TH): distance from couch to the rotation center.

Figure 2 Flowchart of our biological fingerprint verification framework. The biological fingerprint verification process is executed using four major steps: a) geometric correction, b) local feature extraction, c) valid correspondence evaluation, and d) similarity evaluation. The correspondence rate, C, is the similarity index.

Figure 3 Image examples of geometric correction and local feature extraction based on the variation of the top N peaks of local maxima. (a-d) A patient's scout image without any metal artifacts: (a) Original image and (b-d) cropped processing areas of the geometrically corrected images. Yellow circles represent the initial local feature points in the processing area by varying the (b) top-100 peaks, (c) top-200 peaks, and (d) top-300 peaks of the local maxima. (e-h) A patient's scout image with metal artifacts (residual contrast medium in the gastrointestinal tract): (e) Original image and (f-h) cropped processing areas of the geometrically corrected images. Yellow circles represent the initial local feature points in the processing area by varying the (f) top-100 peaks, (g) top-200 peaks, and (h) top-300 peaks of the local maxima.

Figure 4 Example images of genuine and impostor pair analyses at N = 300, X = Y = 16. A follow-up scan (center) and a baseline scan (right) correspond to the same patient pair. All images are cropped to select the processing area and are geometrically corrected. A follow-up (center) and baseline (left) scans correspond to a different patient pair. Yellow circles indicate the initial local feature points in the follow-up scan and the local corresponding points in the baseline scan. Lines connecting pairs of yellow circles in pairs of images are valid corresponding feature points on the genuine pair (cyan lines) and impostor pair (magenta lines). The correspondence rates achieved are 80.6% for the genuine pair and 18.0% for the

impostor pair. (N denotes the number of the initial local feature points, and X and Y denote the rows and columns of the template matrix size, respectively).

Figure 5 Example demonstrating an increased correspondence rate in an impostor
490   pair evaluation at N = 300, X = Y = 16. Follow-up (right) and baseline scans (left) from different patients. Both images have been geometrically corrected. Yellow circles denote the sets of the initial local feature points in the follow-up scan and the local corresponding points in the baseline scan. Magenta lines connecting pairs of yellow circles in the two scans denote valid corresponding feature points. The
495   correspondence rate achieved is 44.3%. (N denotes the number of initial local feature points, and X and Y denote the rows and columns of the template matrix size, respectively).

Figure 6 Example demonstrating low correspondence rate examples for a genuine
500   pair evaluation at N = 300, X = Y = 16. Example demonstrating low correspondence rate examples due to a) translocations in the patient's body posture and b) a patient with metal artifacts (residual contrast medium in the gastrointestinal tract). Follow-up (right) and baseline (left) scans of single patients. Both images have been geometrically corrected. Yellow circles denote the initial local feature points in the
505   follow-up scan and the local corresponding points in the baseline scan. Cyan lines connecting pairs of yellow circles in the two scans denote valid corresponding feature points. The correspondence rates we achieved are a) 15.0% and b) 33.3%, respectively. (N denotes the number of initial local feature points, and X and Y denote the rows and columns of the template matrix size, respectively).

510

Figure 7 Example images for analyses of same and different CT systems at N = 300, X = Y = 16. All three scout CT images are for the same patient and cropped to select the processing area and have been geometrically corrected. A follow-up (center) and a baseline (right) scan are acquired from the single CT system (SOMATOM
515   Sensation 64, Siemens Medical Solutions, Forchheim, Germany). However, only a baseline (left) scan is acquired from different CT system (SOMATOM Definition, Siemens Medical Solutions, Forchheim, Germany). Yellow circles indicate the initial local feature points in the follow-up scan and the local corresponding points in the baseline scan. Lines connecting pairs of yellow circles in pairs of images denote valid
520   corresponding feature points on the same CT system (cyan lines) and a different CT system (green lines). The correspondence rates achieved are 58.7% for the same CT

system and 61.0% for a different CT system. (N denotes the number of the initial local feature points, and X and Y denote the rows and columns of the template matrix size, respectively).

525

Figure 8 Comparison of ROC curve performances for four template matrix sizes at N = 300. The plotted ROC curves correspond to template matrix sizes of 8 × 8 (green line), 16 × 16 (red line), 32 × 32 (blue line), and 64 × 64 (black line). N indicates the number of initial local feature points.
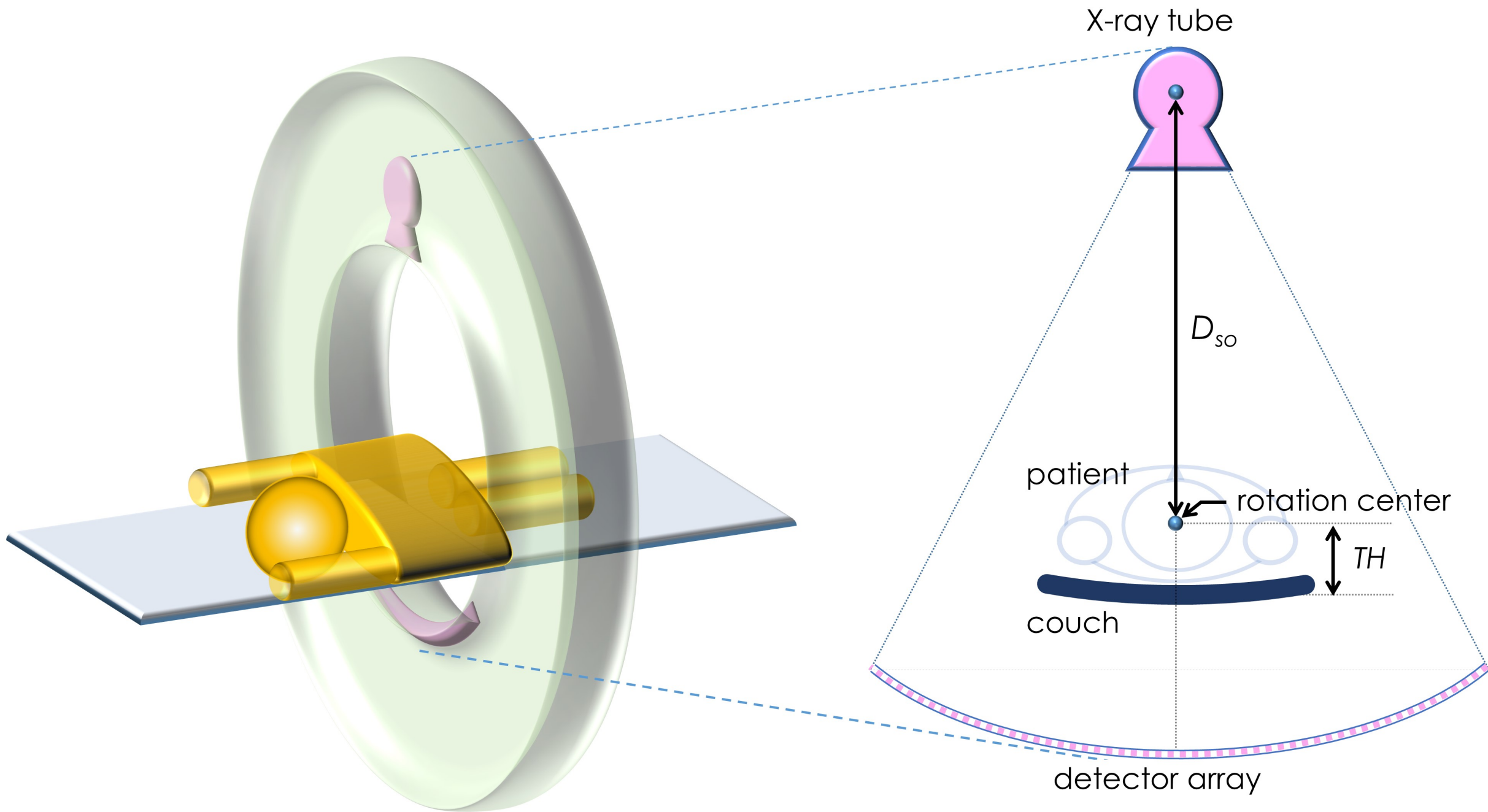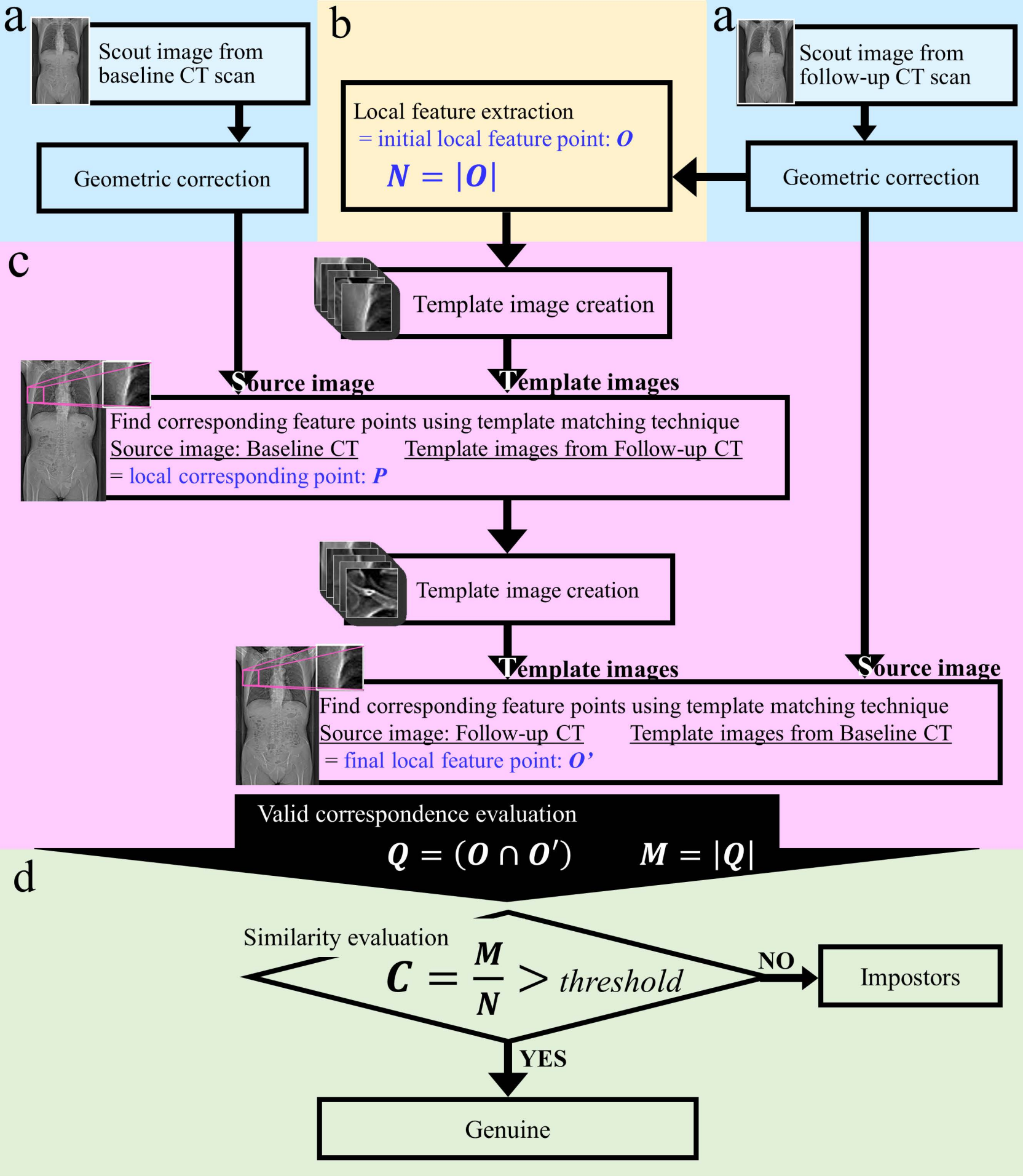
530

Figure 9 Comparison of CMC curve performances for four template matrix sizes at N = 300. The plotted CMC curves correspond to template matrix sizes of 8 × 8 (green line), 16 × 16 (red line), 32 × 32 (blue line), and 64 × 64 (black line). N indicates the number of initial local feature points.

535

Figure 10 Comparison of performance values by varying the number of initial local feature points for four template matrix sizes. (a) Variations of EER for the template matrix sizes of 8 × 8 (green line), 16 × 16 (red line), 32 × 32 (blue line), and 64 × 64 (black line) as a function of the number of initial local feature points. (b) Variations

540 of R1 for the template matrix sizes of 8 × 8 (green line), 16 × 16 (red line), 32 × 32 (blue line), and 64 × 64 (black line) as a function of the number of initial local feature points.

X-ray tube

D_{so}

patient

rotation center

TH

couch

detector array

a

Scout image from baseline CT scan

↓

Geometric correction

a

Scout image from follow-up CT scan

↓

Geometric correction

b

Local feature extraction
= initial local feature point: O

$N = |O|$

c

Template image creation

Source image

Template images

Find corresponding feature points using template matching technique
Source image: Baseline CT   Template images from Follow-up CT
= local corresponding point: P

Template image creation

Template images

Source image

Find corresponding feature points using template matching technique
Source image: Follow-up CT   Template images from Baseline CT
= final local feature point: O'

Valid correspondence evaluation

$Q = (O \cap O')$ $M = |Q|$

d

Similarity evaluation

$C = \dfrac{M}{N} > threshold$

NO → Impostors

YES

↓

Genuine

O : initial local feature point (on the follow-up scout CT image)

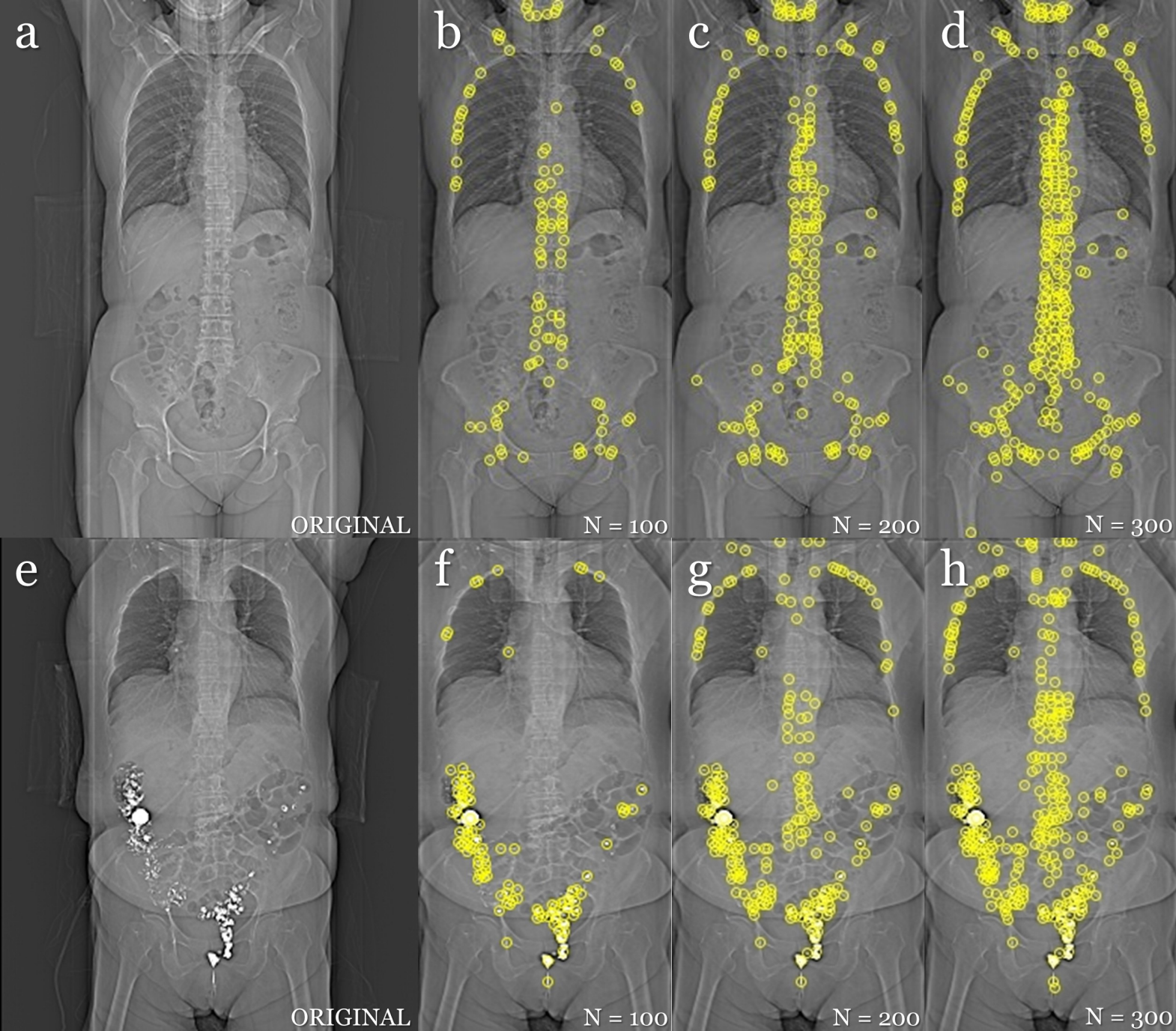N : number of initial local feature point --------------------------------------- $N = |O|$

P : local corresponding point (on the baseline scout CT image)

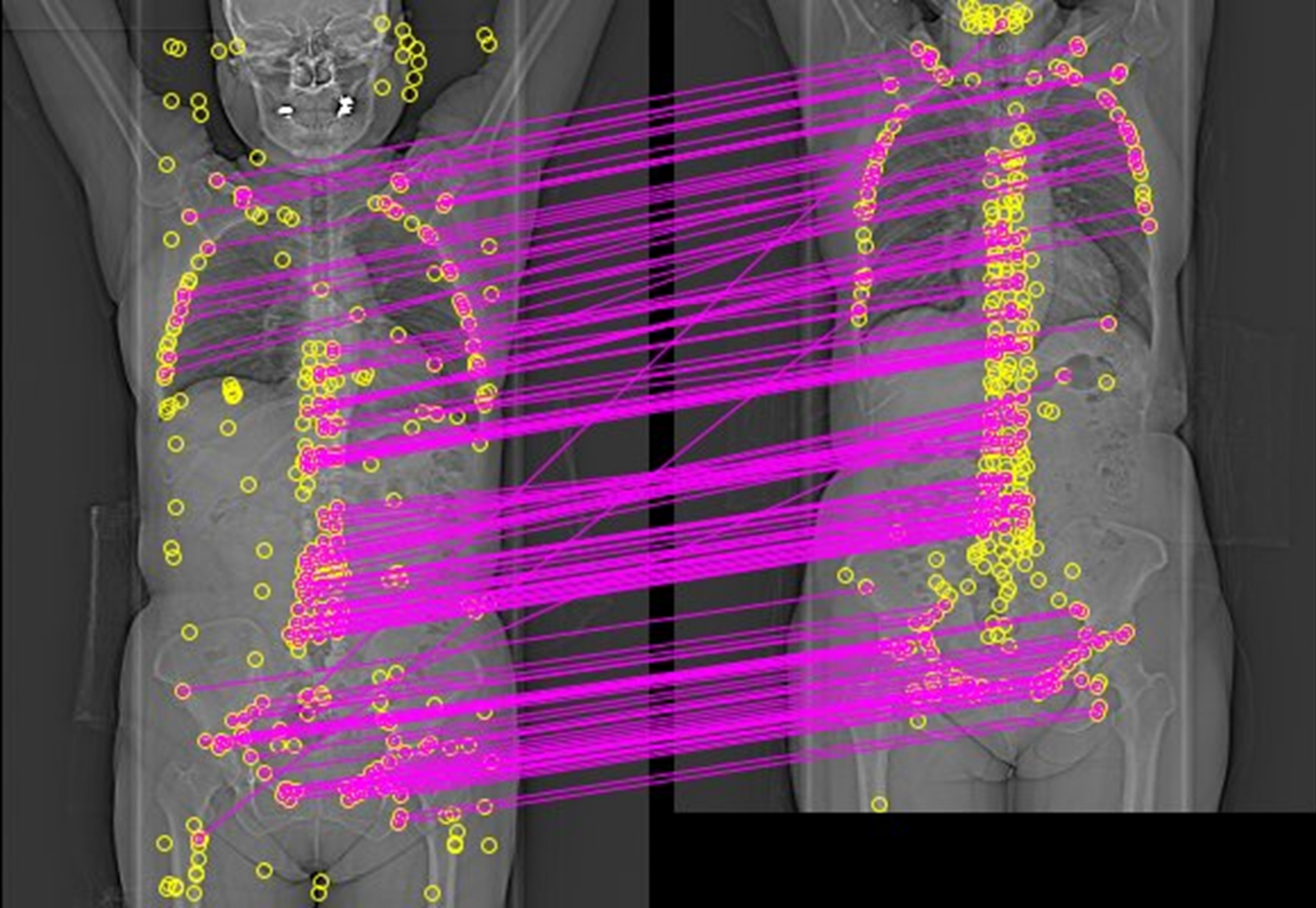O' : final local feature point (on the follow-up scout CT image)

Q : valid corresponding feature point --------------------------------------- $Q = (O \cap O')$

M : number of valid corresponding feature point ------------------------ $M = |Q|$

C : correspondence rate -- $C = {}^{M}/{}_{N}$

a

b

8 × 8
AUC = 0.996
EER = 1.62 %

16 × 16
AUC = 0.998
EER = 1.22 %

32 × 32
AUC = 0.997
EER = 1.68 %

64 × 64
AUC = 0.989
EER = 3.77 %
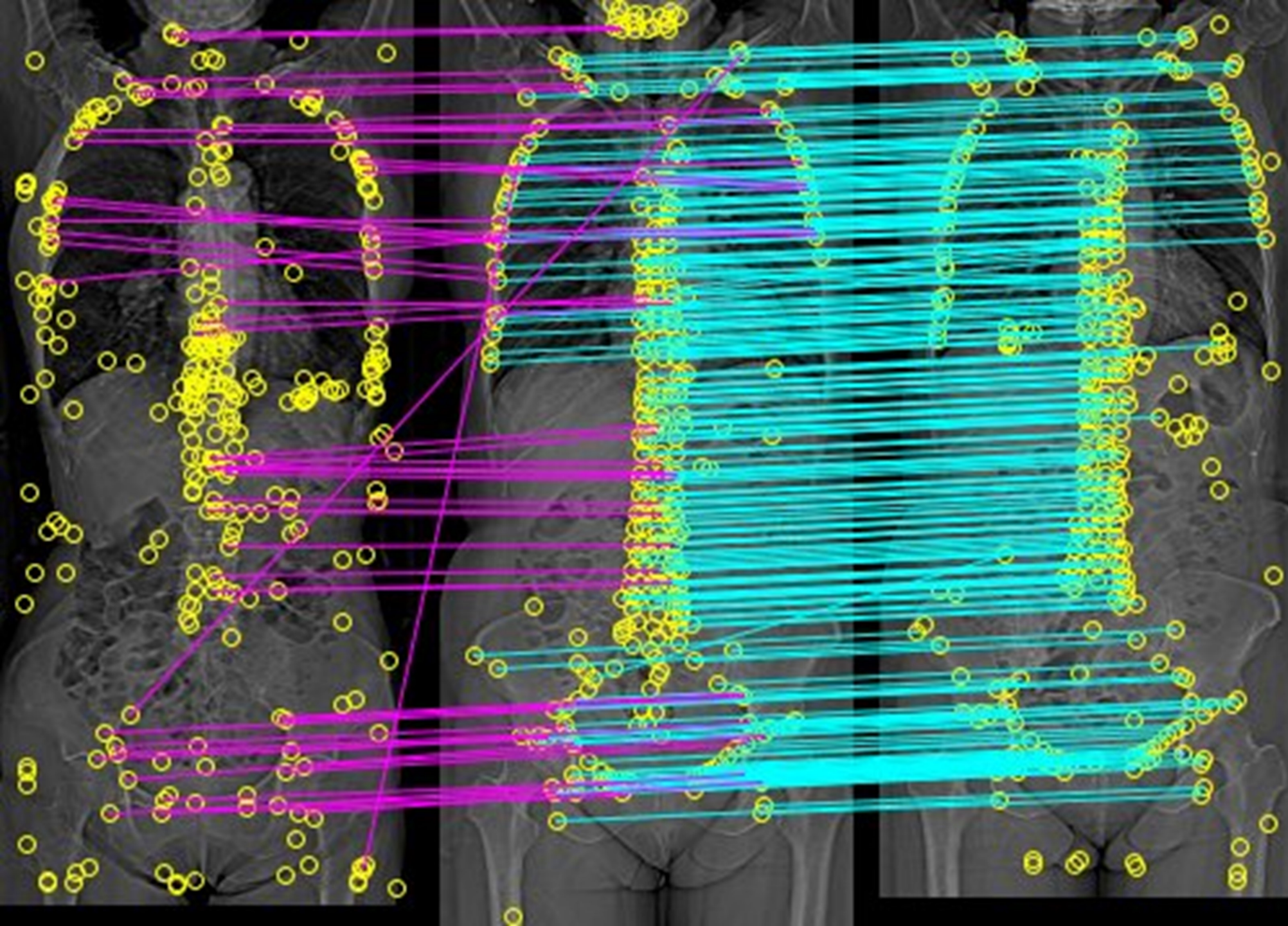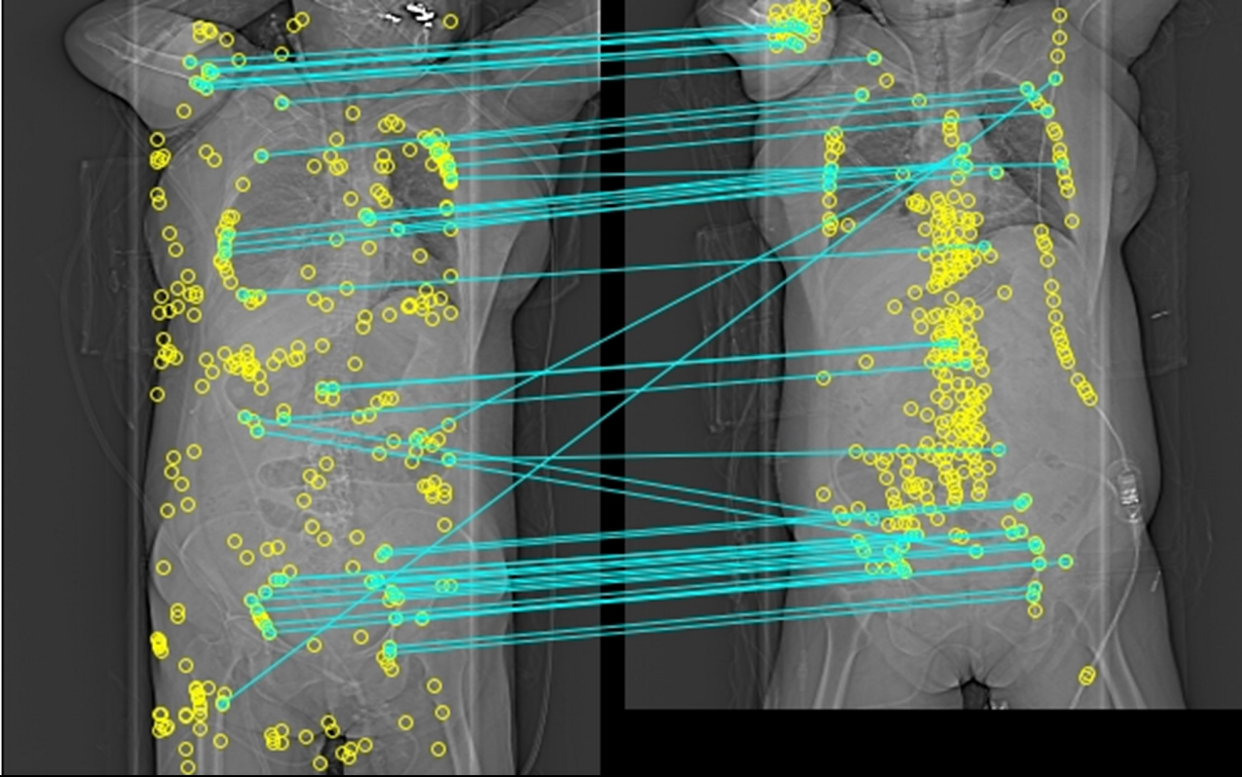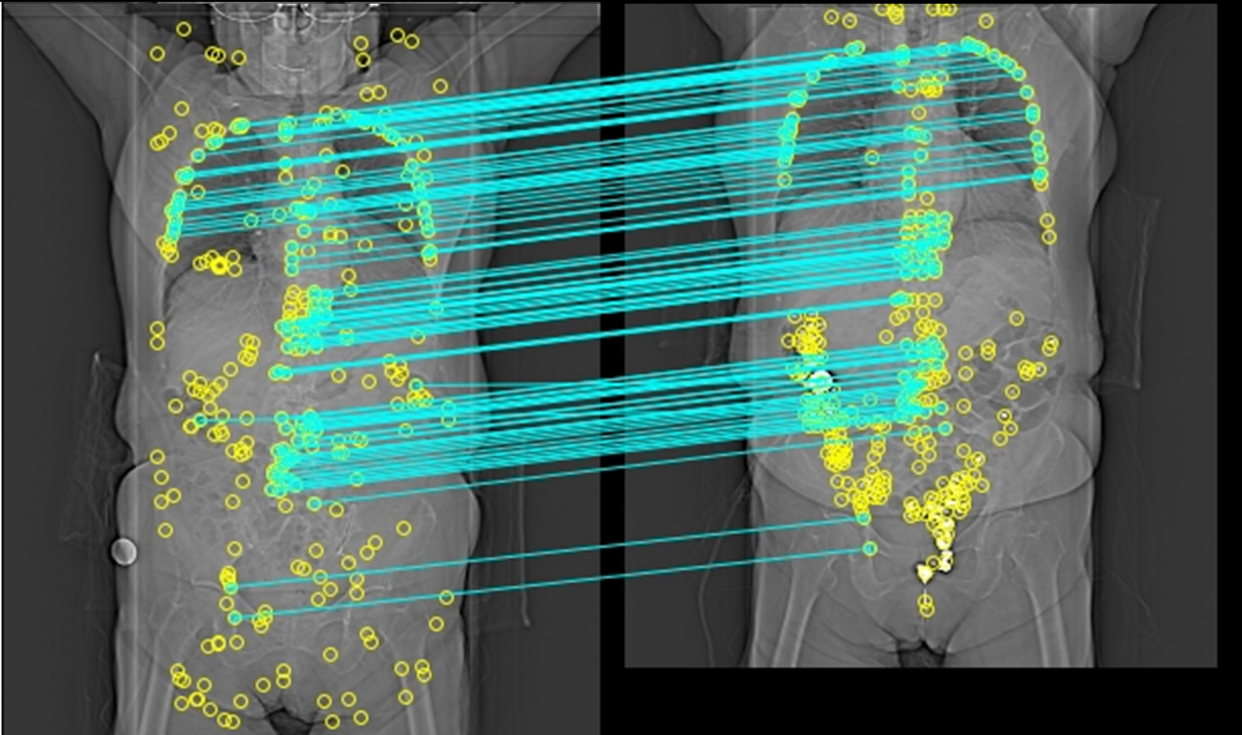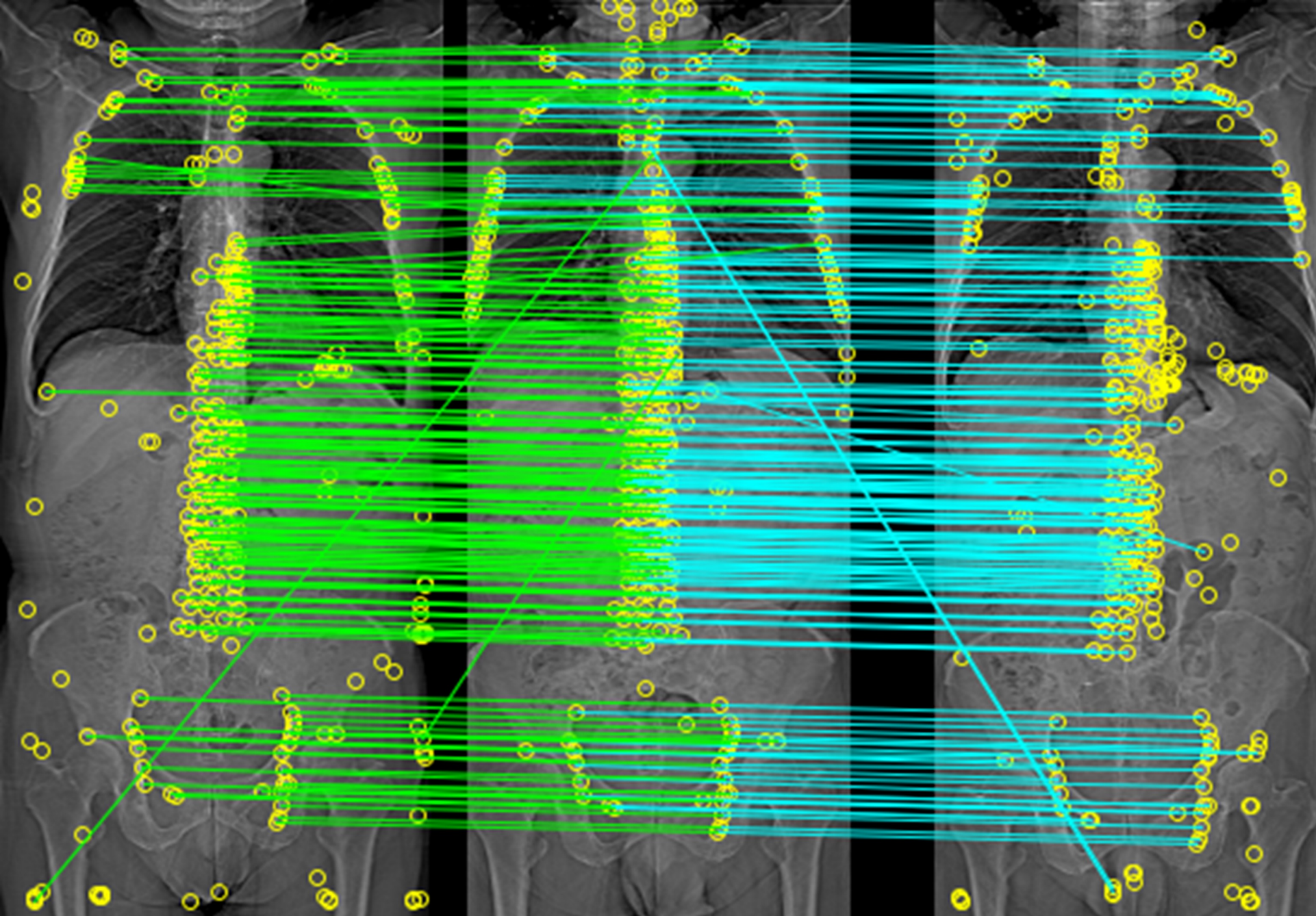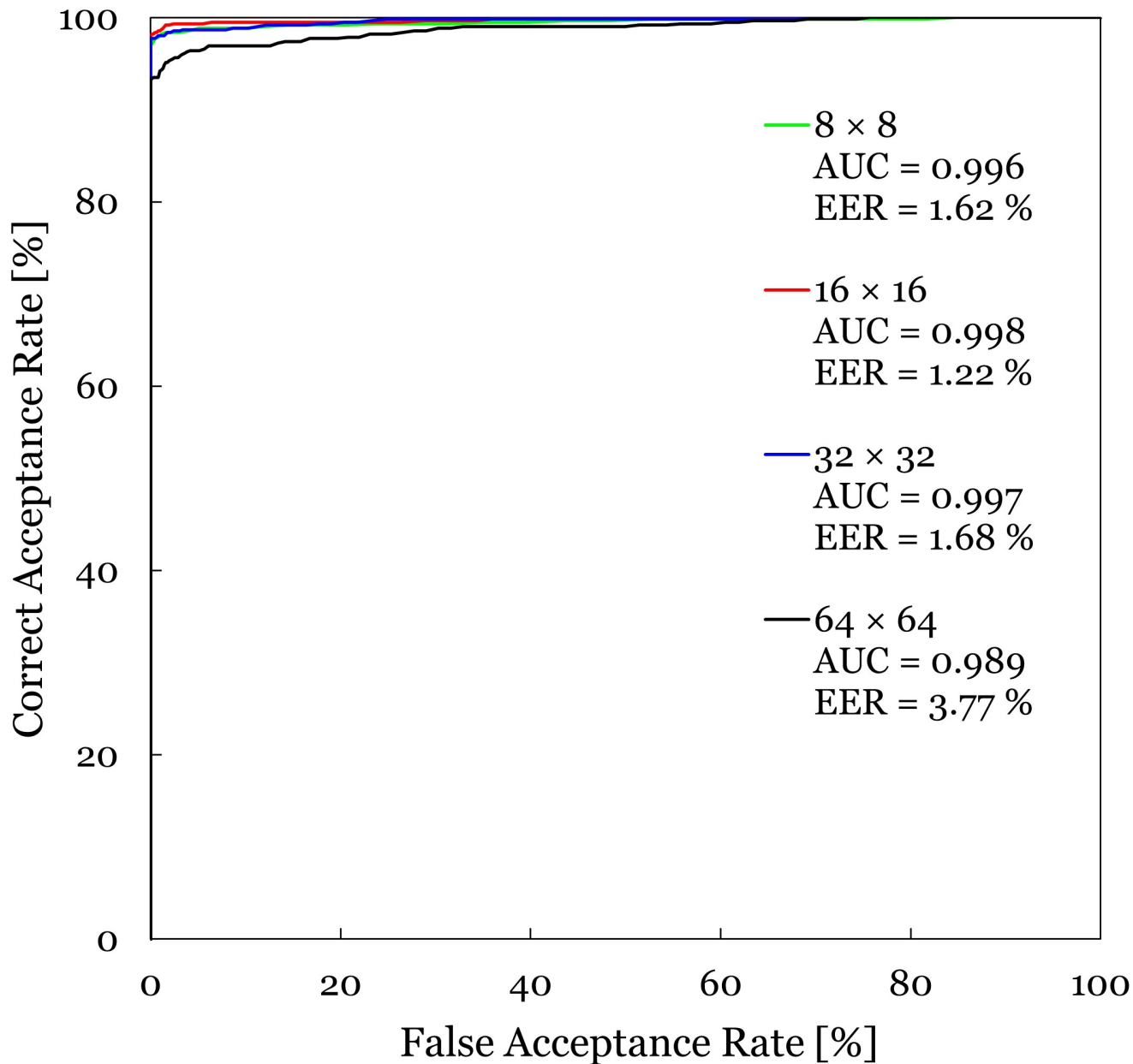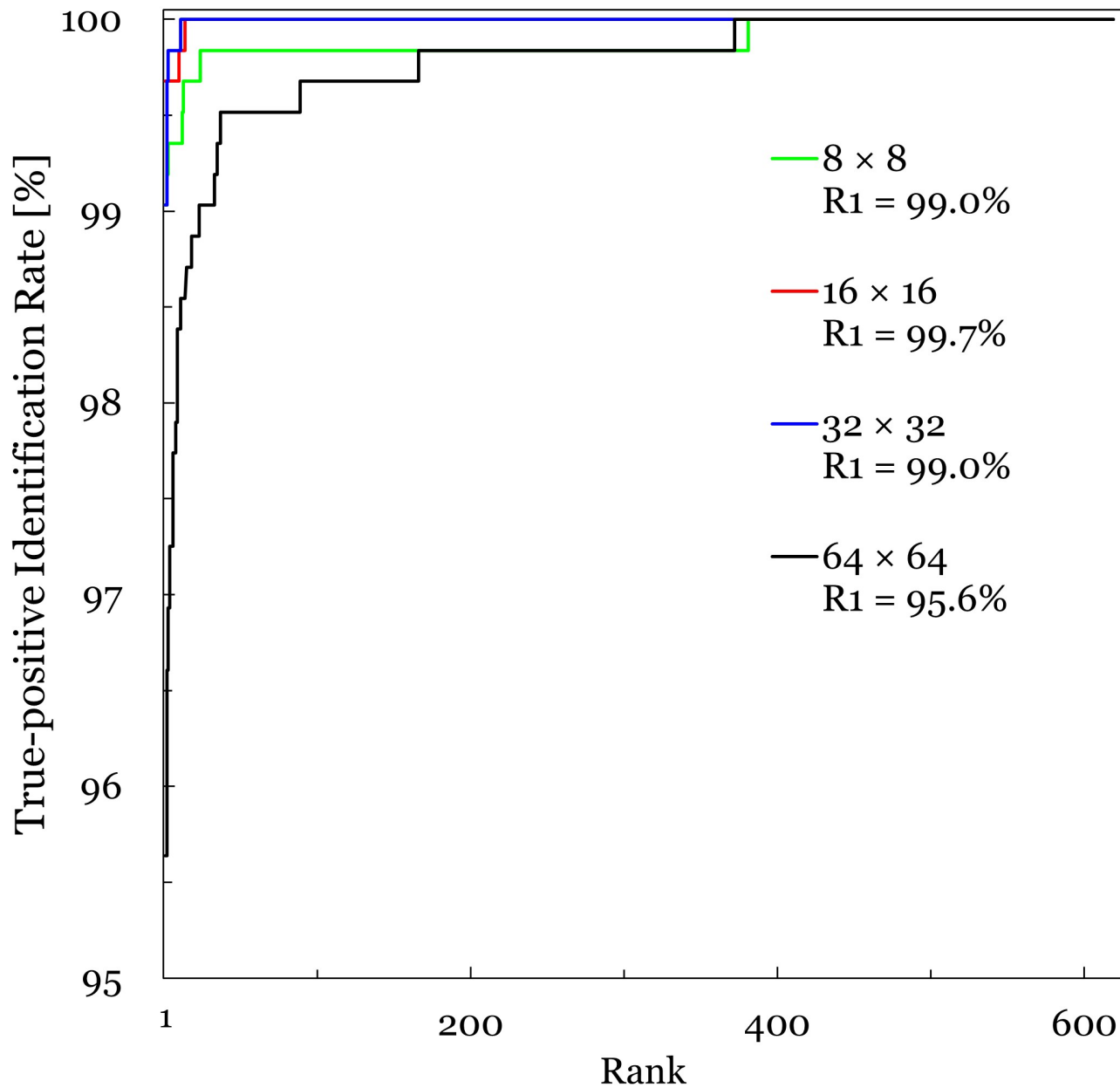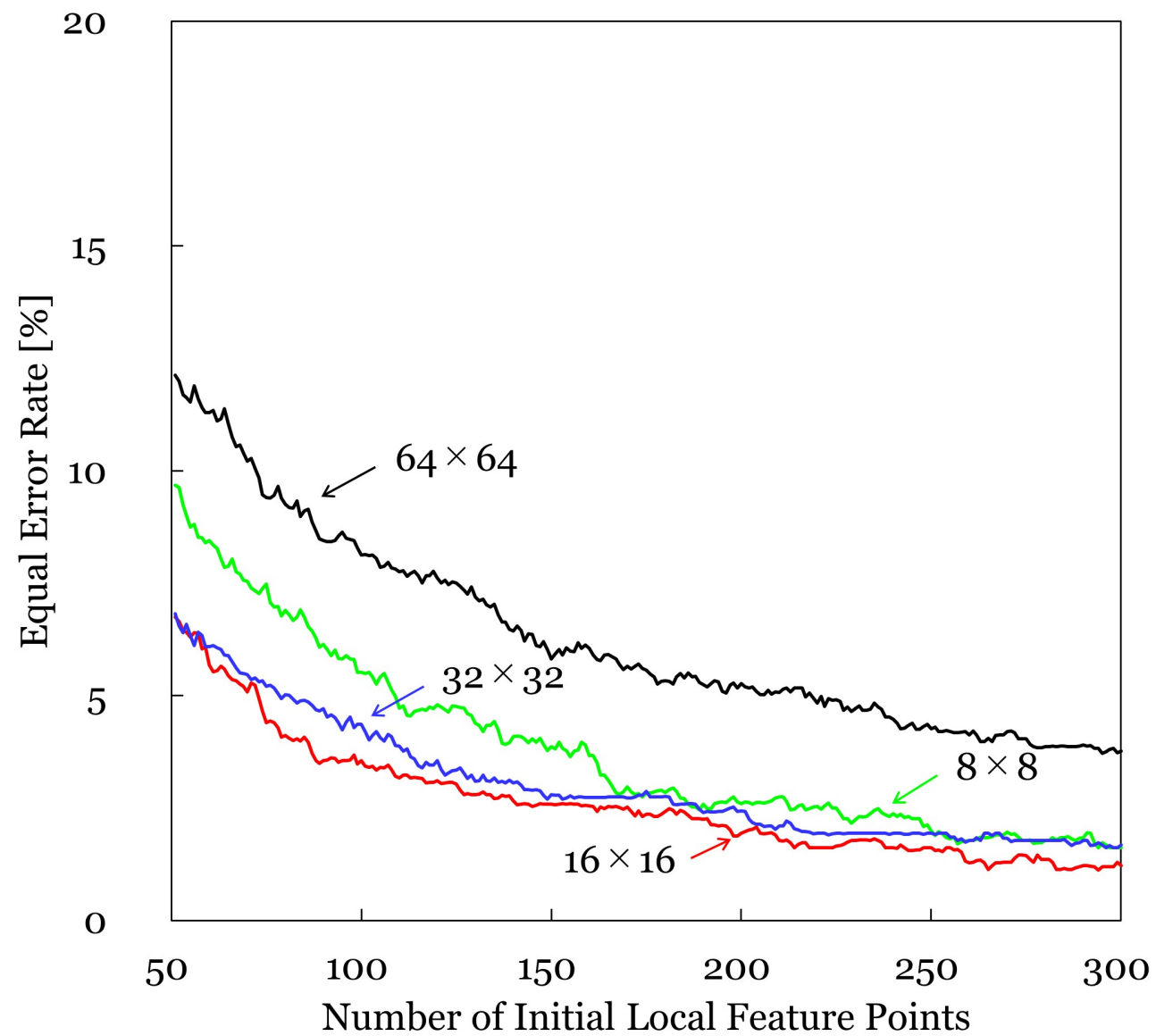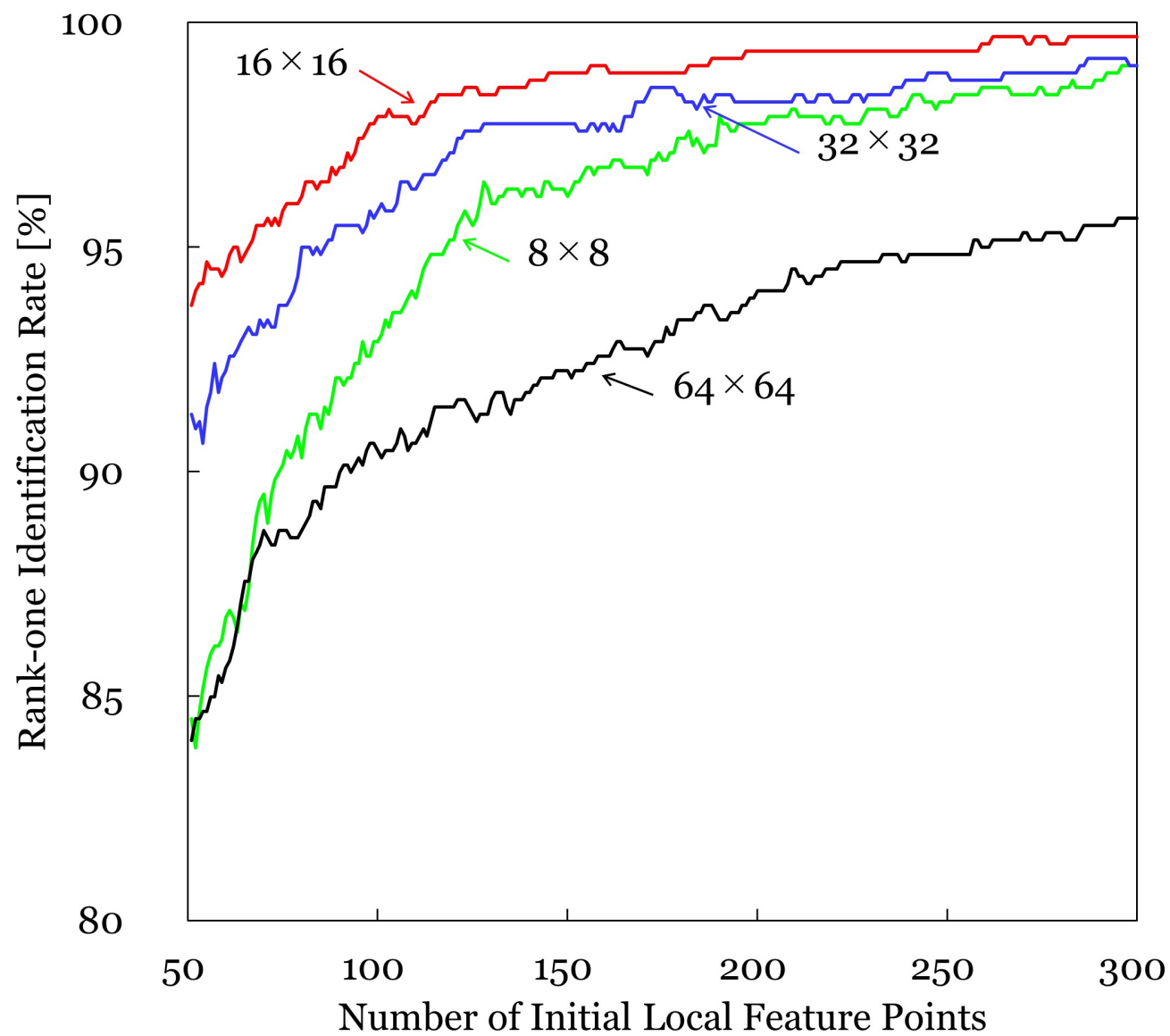
Table I Patient characteristics

Number of patients	619	
Age		
mean ± standard deviation	67 ± 12	years
Range	21 – 92	years
Sex		
Male	383	
Female	286	
scan intervals between the baseline and follow-up examinations		
within 1 week	28	
from 1 week to 1 month	65	
from 1 to 3 months	143	
from 3 to 6 months	236	
from 6 months to 1 year	147	
Table height of scout CT image		
mean ± standard deviation	147 ± 13	mm
Range	111 - 209	mm
Type of artifact including follow-up scout image		
None	364	(299)
Include metal artifact	255	(117)
inside their body	210	(109)
outside their body	30	(7)
Both inside and outside their body	15	(1)

Numbers in parentheses indicate the numbers of artifacts in both the baseline and follow-up scout images.

Table I Scan parameters

Tube voltage	120	kV
Tube current	35	mA
Physical width of the image measured at the rotation center		
Detector size	0.6	mm
Field of view	560	mm

Table I Evaluation of the ROC performance classified by whether the scout CT image includes metal artifacts or not in the follow-up CT scan by varying the number of initial local feature points and template matrix sizes

template matrix size	8 × 8	16 × 16			32 × 32	64 × 64
number of initial local feature points	300	100	200	300	300	300
AUC	with metal artifacts (255)	0.996	0.981	0.980	0.998	0.998	0.986
	without metal artifacts (364)	0.993	0.996	0.996	0.999	0.999	0.993
p-value		0.393	0.0206*	0.0199*	0.488	0.612	0.209

Numbers in parentheses indicate the numbers of patients in each group. Asterisks (*) indicate a statistically significant (p < 0.05) difference in unpaired Delong's test depending on whether a metal artifact was present.